Journal of Luminescence 220 (2020) 116952

Contents lists available at ScienceDirect

Journal of Luminescence

journal homepage: http://www.elsevier.com/locate/jlumin

Optical Properties of InAs Quantum Dots/GaAs Waveguides for Ultra-fast Scintillators

K. Dropiewski [a], A. Minns [a], M. Yakimov [a], V. Tokranov [a], P. Murat [b], S. Oktyabrsky [a,*]

[a] SUNY Polytechnic Institute, 257 Fuller Rd, Albany, 12203, USA
[b] Fermi National Accelerator Laboratory, PO Box 500, Batavia, 60510, USA

A B S T R A C T

InAs Quantum Dots (QDs) embedded in a GaAs matrix have unique scintillation properties, valuable for high-energy physics and medical applications. Temperature-dependent photoluminescence, waveguide attenuation and alpha particle response measurements were employed to analyze the optical properties of a 25 μm thick waveguiding scintillator. Optimizing the electrostatics of the QD layered structure with p-type modulation doping resulted in QD photoluminescence (PL) efficiency as high as 60% at room temperature. Analysis of attenuation of the QD waveguide showed surface scattering predominated over the first 2–3 mm of light propagation and low (~1 cm^{-1}) self-absorption was more significant at longer distances, after the decay of high order modes (high angle light rays). Responses to 5.5 MeV alpha particles from the integrated photodiode on top of the QD scintillator/waveguide (QD/WG) show an extremely fast (300 ps) decay constant, and a 70 ps time resolution (limited by circuit noise and bandwidth) with a collection efficiency of 17,000 photons per 1 MeV of deposited energy.

1. Introduction

Recently, waveguiding quantum dot (QD) semiconductor nanostructures were proposed as a medium for high-efficiency, picosecond time resolution scintillators [1], which are greatly sought after for many applications in high-energy physics and medical imaging. Such ultra-fast scintillators are needed for improved timing of subatomic particle observations in high-energy physics and calorimetry [2] and for more precise time-of-flight information in medical imaging, which reduces patient exposure to ionizing radiation [3]. While significant improvements have been made to incorporate time-of-flight capability into PET imaging [4–6], inorganic scintillators currently operate close to their limits [7–10]; therefore new approaches are in high demand.

Semiconductor scintillating materials, such as doped II-VI compounds, have exceptional light yield and are used in many applications. However, they are limited as scintillators by relatively slow luminescence, and also by the combination of high self-absorption and low material density. These last two factors mean semiconductor scintillators, when designed as thick slabs to enable stopping of high-energy particles and photons, emit light that can be absorbed (reducing overall efficiency) and re-emitted (leading to longer decay times), which are collectively known as photon recycling. Instead, InAs QDs (acting as luminescence centers) embedded in a GaAs matrix can be designed to minimize optical self-absorption: a low density of QDs (~10^{15} QDs/cm^3) limits QD self-absorption, and the red-shift of the QD ground state with respect to the GaAs matrix band edge (~300 meV) drastically reduces absorption in GaAs. This ultimately decreases photon recycling effects, which reduces the decay time of InAs QDs, making them a uniquely fast scintillation detector material [1]. Using the embedded QDs as luminescence centers, this material can have high efficiency conversion of radiation energy, fast radiative recombination in the strongly localized potential of the QDs, and fast capture of electrons due to the high mobility of GaAs. The unique alpha particle response properties of this integrated scintillator have been demonstrated in a previous work [11].

We present major considerations to improve the efficiency of this ultra-fast, high photon yield, room-temperature semiconductor scintillator, composed of InAs QDs acting as luminescence centers, embedded within a GaAs matrix acting as the stopping material. The full detector consists of a scintillation sensor, which also serves as a waveguide, and a photodetector, both of which are monolithically integrated and later transferred to a substrate with a low refractive index. GaAs has several beneficial qualities as a radiation stopping material: a direct band gap with very high maximum photon yield (~240,000 photons/MeV), a reasonable radiation length (2.3 cm), and high electron mobility (up to 8500 cm^2/V at low doping). The high mobility results in fast transport and capture of electrons in the QDs (~2–5 ps) [12–14].

Due to the high refractive index (n = 3.5) of the GaAs matrix, light extraction through a semiconductor/air interface is very inefficient [16]: just $(2n)^{-2}$, or 2%, of the light is transmitted through a planar interface with air. The rest is captured via total internal reflection. The

* Corresponding author.
E-mail address: soktyabrsky@sunypoly.edu (S. Oktyabrsky).

https://doi.org/10.1016/j.jlumin.2019.116952
Received 17 July 2019; Received in revised form 29 November 2019; Accepted 4 December 2019
Available online 5 December 2019

coupling of light to an external photodetector (PD) is a well-known challenge; however, in case of III-V epitaxial films, a natural solution for light extraction is to monolithically integrate a photodiode with the scintillator. As a result of that, the high refractive index becomes beneficial as the scintillator can now be processed into a waveguide (WG), and the coupling efficiency between the scintillator and the PD is not limited by the high index-contrast interface. The QD emission is red-shifted by ~300 meV from the GaAs bandgap due to the narrow bandgap of InAs being modified by strain and quantum confinement [15], resulting in low self-absorption.

2. Methods

The structures studied were grown using molecular beam epitaxy (MBE) on GaAs(001) substrates. A diagram of the epitaxial layers, explaining the layout of both the QD scintillator/waveguide (QD/WG) and the monolithically integrated photodiode (PD) is shown in Fig. 1. The entire detector structure is grown on a 100 nm thick AlAs sacrificial layer to allow transfer to a lower refractive index substrate (e.g. glass) using the epitaxial lift-off method [17]. A variable composition layer of $Al_{0.3\text{-}0.1}Ga_{0.7\text{-}0.9}As$ is grown on both sides of the QD/WG as a barrier to reduce photocarrier surface recombination. Fig. 1 shows a 25 μm thick WG containing 62 sheets of InAs QDs grown at 515 °C separated by 400 nm layers of GaAs matrix grown at 590 °C. The 400 nm spacing was chosen as a first pass at optimization. By maximizing the spacing, the QD bulk density and related self-absorption were reduced while maintaining a high built-in electric field between the QD layers, which reduced electron drift time to a few picoseconds.

An integrated scintillation detector includes the QD scintillator/waveguiding structure and an InGaAs p-i-n PD (Fig. 1(b)), tuned to the QD emission wavelength. To maintain low PD capacitance, the PD area was limited to 0.021 mm^2 (WG-QD1) and 0.029 mm^2 (WG-QD2), resulting in an estimated capacitance of 3 pF and 4.3 pF respectively. This was accomplished by etching the PD structure off from most of the WG area as is indicated in Fig. 1.

Each QD sheet was prepared by MBE growth of ~2 monolayers (MLs) of InAs, which self-assembled into QDs on a GaAs surface via Stranski-Krastanov nucleation of 3-dimensional islands with a wetting layer (Fig. 2). After nucleation, the QDs were immediately capped with ~2 MLs of AlAs. This capping layer prevents evolution of the QDs on the growing surface, improves QD volume uniformity and thus luminescence efficiency [18], and reduces the wetting layer states as discussed below. Scanning transmission electron microscopy (STEM) images (Fig. 2) were evaluated to determine that the average lateral diameter of QDs is 17 nm and the QD density is (3–5)x10^{10} cm^{-2} per sheet. Fig. 2(b) presents a high magnification STEM micrograph of the QDs and the wetting layer, which consists of InAs and AlAs capping. The detailed structure and importance of this design is discussed below.

The WG was p-type modulation doped to positively charge QDs for better collection of photoelectrons and had barriers on the top and bottom of the WG, composed of the wide-bandgap material AlGaAs, to prevent electron surface recombination. Test QD samples with 1 modulation doping layer (labelled QD1 in Figs. 3 and 4) and 3 modulation doping layers (labelled QD2, QD3) were evaluated using photoluminescence (PL). Another test sample (QD4) contained QDs capped with a 2 ML AlAs layer placed inside a ~6 nm $In_{0.06}Ga_{0.94}As$ quantum well (QW) ("dot in the well" design), which red-shifted the QD ground state energy [13].

The PD was composed of a p+-type contact of 300 nm $In_{0.35}Ga_{0.65}As$, an absorber of 700 nm $In_{0.35}Ga_{0.65}As$, and an n+-type contact of 400 nm $In_{0.35}Ga_{0.65}As$, all grown at 450 °C. The PD structure was epitaxially grown on a graded metamorphic buffer (MB) layer containing 700 nm of $Al_{0.92\text{-}0.6}In_{0.03\text{-}0.35}Ga_{0.05}As$ grown at 350 °C, to relieve mismatch strain via dislocations. The bandgap of the PD absorber was adjusted to 0.95 eV at room temperature, which is estimated to absorb roughly 50–60% of 1170 nm photons at normal incidence. The detector PD was fabricated using two lithography masks to form a photodetector mesa and metallize the contacts. After processing, most of the structure is a long, narrow QD/WG stripe with a small area PD on the top surface. The integrated scintillation detector was separated from the GaAs substrate and transferred to a low refractive index material to evaluate timing and energetic characteristics with ^{241}Am as an excitation source.

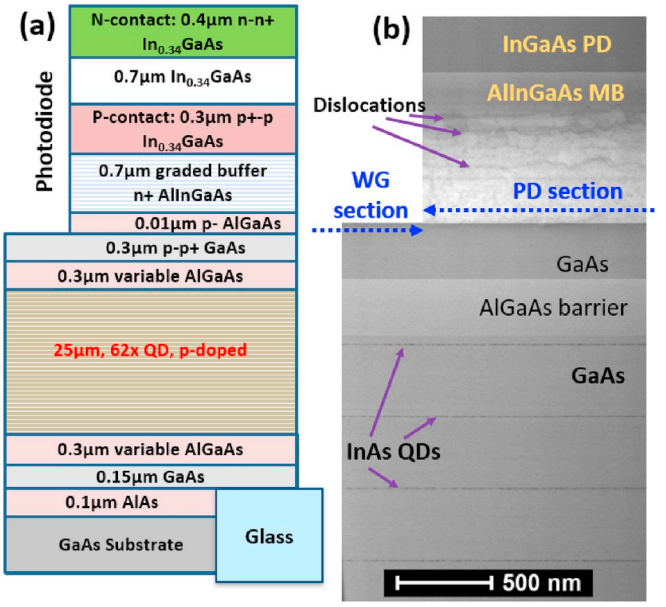

Fig. 1. (a) Diagram of an MBE grown structure that includes InAs QD/GaAs waveguide (WG) and InGaAs photodiode (PD) on top. The structure is grown with MBE on GaAs(001), separated from the substrate, and transferred to a glass slide by the epitaxial lift-off method. (b) STEM bright field cross-sectional image of the top of the QD waveguide and metamorphic buffer (MB) separating QD/WG and InGaAs PD.

3. Results and discussion

3.1. QD waveguide electrostatics

Engineering an electrostatic potential is a powerful method to

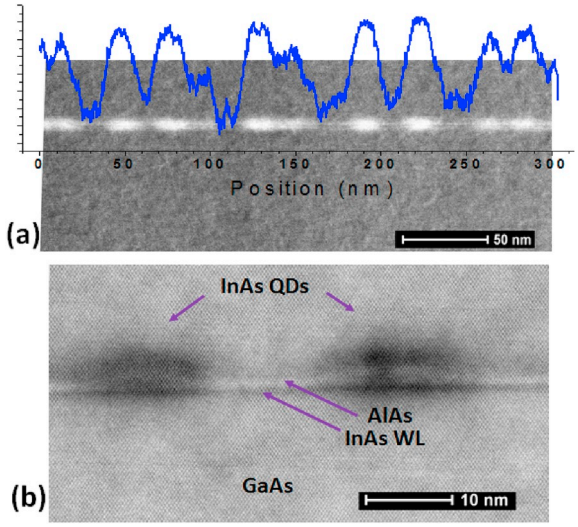

Fig. 2. (a) High-angle annular dark-field (HAADF) cross-sectional micrograph of a QD layer with associated contrast. (b) STEM HAADF micrograph of two InAs QDs and the wetting layer (WL) between them.

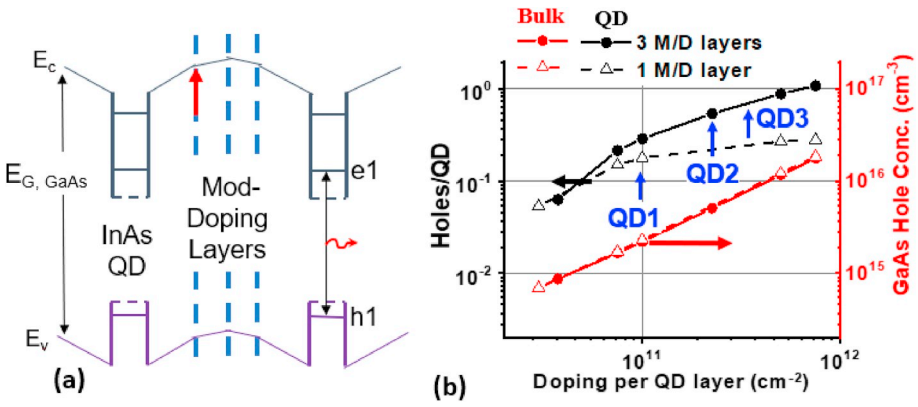

Fig. 3. (a) Equilibrium band diagram along the growth direction of a modulation doped QD structure with three doping layers, showing band bending due to hole accumulation in QDs. (b) Calculated room temperature QD occupation and bulk hole concentration vs. total modulation doping per QD layer, for single sheet modulation doping (MD) and 3x-sheet MD structures. Arrows labelled "QD1" and "QD2"/"QD3" indicate doping of three experimental scintillation samples with single- and triple-sheet MD layers, respectively.

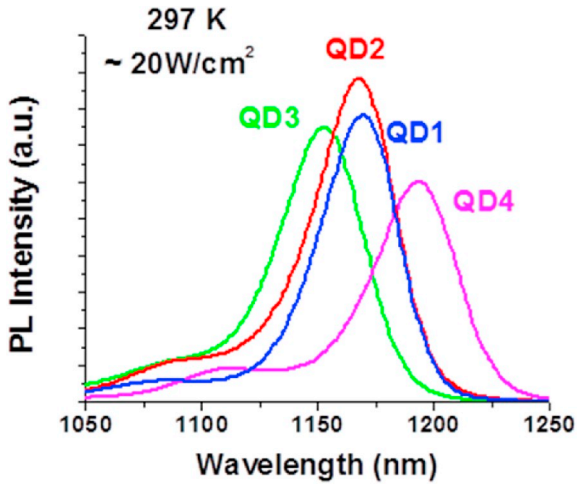

Fig. 4. Room temperature photoluminescence spectra of four samples: reference (QD1), 2.3× increased doping in 3 MD layers (QD2), 3.8× increased doping in 3 MD layers (QD3), and QDs on InGaAs QW with reference doping (QD4).

control the capture of charge carriers in QDs [19,20] and the luminescence efficiency at low excitation levels. As the effective mass of electrons in GaAs ($m^* = 0.067m_e$) is ~7 times less than that of holes, the dynamics of minority electrons are significantly faster and were the focus of our optimization. Both the electron drift times (towards the QDs) and recombination times can be minimized by p-type modulation doping [21], where a thin layer of GaAs with acceptor (carbon in our case) doping is grown some distance from the QD sheets. In p-type modulation doped (MD) structures holes are captured in the QDs, generating attractive potential for electrons around the dots (Fig. 3(a)), increasing the capture rate of minority electrons and the rate of recombination.

MD was optimized for higher doping levels, which increase the drift field between the QD layers, and lower density of free holes in the GaAs matrix, which may raise free carrier absorption and recombination in the bulk. One of the envisioned approaches comprises multiple modulation doped layers, as this reduces the bulk hole concentration. Fig. 3(b) compares calculated probabilities of QD occupation by holes and bulk hole concentration in single-sheet and triple-sheet (as in Fig. 3(a)) modulation doped structures. By distributing dopants through three sheets, we were able to double the QD charge and reduce bulk hole concentration, specifically when the doping levels are in the range of 2–10 acceptors per dot. These calculations were performed using a one-dimensional Poisson solver which did not consider the randomness of QDs within their growth plane. The calculation assumed the QD ground-state hole level is 195 meV above the valence band of GaAs [15] and a hole level degeneracy of 4.

We prepared QD test samples as well as thick waveguiding samples (as in Fig. 1) of two different modulation doping profiles. The sample labelled "QD1" had a single 10 nm modulation doping layer with 10^{11} cm^{-2} carbon acceptors. In "QD2", three 5 nm thick layers of identically doped GaAs, separated from each other by 100 nm of undoped GaAs, were grown in the middle between InAs QD sheets, with a total doping of 2.3×10^{11} cm^{-2} ("QD2" in Fig. 3(b)).

4-point probe resistivity measurements of the QD1 and QD2 waveguides, separated from the substrate, gave 0.9 Ω·cm and 0.7 Ω·cm. This corresponds to a bulk hole density of 1.3×10^{16} cm^{-3} and 2.3×10^{16} cm^{-3}, slightly higher than calculated in Fig. 3(b), but likely due to unintentional background doping of GaAs matrix. At this concentration, the radiative recombination in the bulk is still very low, and that is indicated by the difference between the GaAs PL intensity (at 870 nm) and the QD PL intensity, adifference of 2–3 orders of magnitude.

It is worth evaluating the built-in electric field between the QD layers and the subsequent electron drift time, as it directly affects the timing resolution. For this estimation, the field value at the first doping layer of QD2 (indicated by the arrow in Fig. 3(a)) and the only doping layer in QD1 is calculated from the electrostatic modeling as ~5 kV/cm. This results in an electron taking ~1 ps to drift between the QD layers, significantly below the measured electron capture times in QDs: ~5–10 ps [12,13,22,23].

3.2. Temperature-dependent photoluminescence

Fig. 4 compares room temperature photoluminescence (PL) spectra of the thin QD samples: QD1 (10^{11} cm^{-2} doping in one MD layer), QD2 (2.3×10^{11} cm^{-2} doping in 3 MD layers), QD3 (3.8×10^{11} doping in 3 MD layers), and QD4 (QDs in an InGaAs QW). Thin samples contain only 3 layers of QDs. The excitation source was an unfocused 50 mW red (650 nm) semiconductor laser providing ~20 W/cm^2 of intensity on the top surface of the sample. PL was collected in a reflection geometry, dispersed by a 0.5 m monochromator and measured using a p-i-n InGaAs photodiode.

Samples QD1-3 had very similar InAs QDs, which is illustrated by the similar shapes and position of the spectral bands. The 12 nm blue shift of the PL band of the QD3 sample is the result of slightly higher (~5 °C) MBE growth temperature.

Samples QD1-3 were capped by ~2 monolayers (ML) of AlAs, intended to increase the barrier for thermal escape of the carriers and stabilize their size and shape, which also red-shifted the PL peak (1168 nm) when compared to uncapped QD samples [18]. Additionally, the QDs in QD4 were grown inside an InGaAs QW, which red-shifted the PL peak even further than in QDs 1–3; this was expected to improve thermal stability [13].

Fig. 5(a) shows the evolution of PL spectra of the QD2 sample at

temperatures ranging from 77 K to 463 K. The shift of the PL peak is due to bandgap reduction at higher temperatures. QD excited state luminescence, which is blue-shifted with respect to the principal ground-state PL peaks, was more pronounced at elevated temperatures due to their higher occupation.

Thermal quenching of the integrated PL intensity of samples QD1-4 is shown in Fig. 5(b). The PL efficiency dropped quickly at higher temperatures and saturated at low temperatures. This behavior is commonly observed in QD structures, where the internal luminescence efficiency approaches unity at low temperatures due to fast capture and strong localization of photocarriers in the QDs [23].

QD4, with an InGaAs QW, has deeper QD states compared to QD1. QD4 showed only a marginal improvement to thermal stability at higher temperatures, but slightly reduced intensity at room temperature (RT) (Fig. 4). Therefore, though not entirely discounted, the QD4 design was ruled out for use in the thick waveguide structures in part because the extra In-containing layers required additional evaluation of the introduced strain and self-absorption.

The 2.3× doped sample (QD2) exhibited the best thermal performance, with roughly 20% PL efficiency at 463 K, and 60% PL efficiency at room temperature (RT) compared to ~40–50% for QD1, QD3 and QD4. Increased p-type modulation doping improves the temperature stability of PL by increasing the occupancy of the QD hole states (Fig. 3 (b)). This effect is well-known from QD lasers, where higher occupancy reduces the thermal spreading of holes over the closely spaced hole energy levels in QDs [24].

It should be noted that the PL thermal quenching effect is most likely due to non-radiative recombination of minority electrons in defective QDs [23]. At room temperature, thermal escape rate is significantly faster than the QD recombination rate, and the electrons spend a small fraction of their lifetime in the barrier. The fact that the bulk GaAs PL (870 nm at RT) is still an order of magnitude less than the QD PL intensity, even at 463 K, confirms that the electron capture rate of the QDs is higher than the escape rate from the QDs, and that both rates increase with rising temperature [23]. In this case, recombination in QDs dominates, although it is primarily radiative below RT and becomes non-radiative (in defective QDs) at higher temperatures. The details of the photoelectron kinetics in QD systems have been studied elsewhere [23].

3.3. QD waveguide attenuation

Evaluating the waveguiding properties of InAs QDs in a GaAs matrix requires some unusual considerations: firstly, it has relatively high QD self-absorption (for a waveguide) and possible free carrier absorption, depending on doping. Secondly, it is massively multimodal to maximize energetic photon and particle absorption during scintillation, which results in a waveguide with multi-wavelength thickness. In fact, a 20 μm thick GaAs waveguide (WG) supports over 10^6 waveguiding modes [25], making it more efficient to consider light ray bouncing within the WG than individual modes. Higher-order modes (higher-angle reflecting light rays) are more sensitive to self-absorption, light scattering, and surface scattering, thereby creating additional technological challenges. To address and evaluate these considerations, some baseline properties of the QD waveguide are measured and analysed using a simple geometrical optics model.

Waveguide attenuation measurements were taken using an experimental setup as shown in Fig. 6(a). QD WGs using QD1 and QD2 designs were made 20 μm and 25 μm thick respectively. The QD/WGs were grown as shown in Fig. 1 but without a photodiode, after which they were transferred from the GaAs substrate to a glass slide. The resultant WGs were excited by a red (650 nm) semiconductor laser, focused to a spot diameter of <50 μm. PL spectra were collected using a multi-mode fiber with an acceptance angle of 13°, coupled to the edge of the WG, as the excitation source was moved away from the WG edge. PL spectra attenuation as a function of waveguiding length ("*x*" in Fig. 6(a)) from the two waveguiding samples with QD1 and QD2 designs are shown in Fig. 6(b and c), and the integrated PL as a function of waveguiding length is plotted in Fig. 7. The spectra of both samples share two major features. Firstly, stronger luminescence decay at shorter wavelengths, corresponding to transitions between excited QD states at 1050–1150 nm (ES in Fig. 6) compared to the QD ground state (GS in Fig. 6). Secondly, the decay slows down at longer waveguiding lengths when both the shape and intensity of the luminescence band stops changing, also illustrated in Fig. 7 as a flattening of the integrated PL signal. WG-QD1 and WG-QD2 have very similar QDs, shown in Fig. 4, and one significant feature of these QDs is a relatively large separation between the excited and ground states, about 90 meV as estimated from the spectra. This large separation effectively reduces spreading of the electron spectrum and is one of the reasons for the high thermal stability of devices with QDs, such as laser diodes [26].

Integrated PL intensity as a function of the waveguiding length is shown in Fig. 7 for the waveguiding samples WG-QD1 and WG-QD2. The attenuation is also similar but is not exponentially dependent on the waveguiding length. To understand the mechanisms of attenuation, light propagation in the WG was simulated using a ray optics approximation assuming total internal reflection (TIR) from the WG surfaces. In Eq. (1), attenuation of light due to QD self-absorption is described such that the luminescence or scintillation produces photons in the entire 4π of solid angles, and that both the forward and backward (reflected from

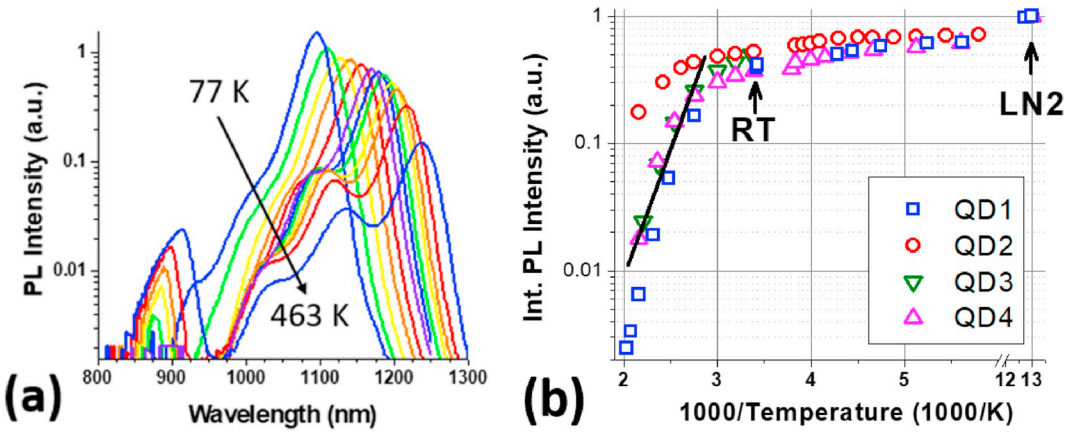

Fig. 5. (a) PL spectra (log scale) of QD2 sample with the best quenching properties from 77K to 463 K. Shift of the PL peak is due to bandgap reduction with temperature. (d) Arrhenius plot of integrated PL intensity as a function of temperature for the QD test samples. Intensities are normalized to unity at the temperature of liquid nitrogen (LN2). The solid line shows an activation energy of 400 meV. LN2 and room temperature (RT) are indicated with arrows.

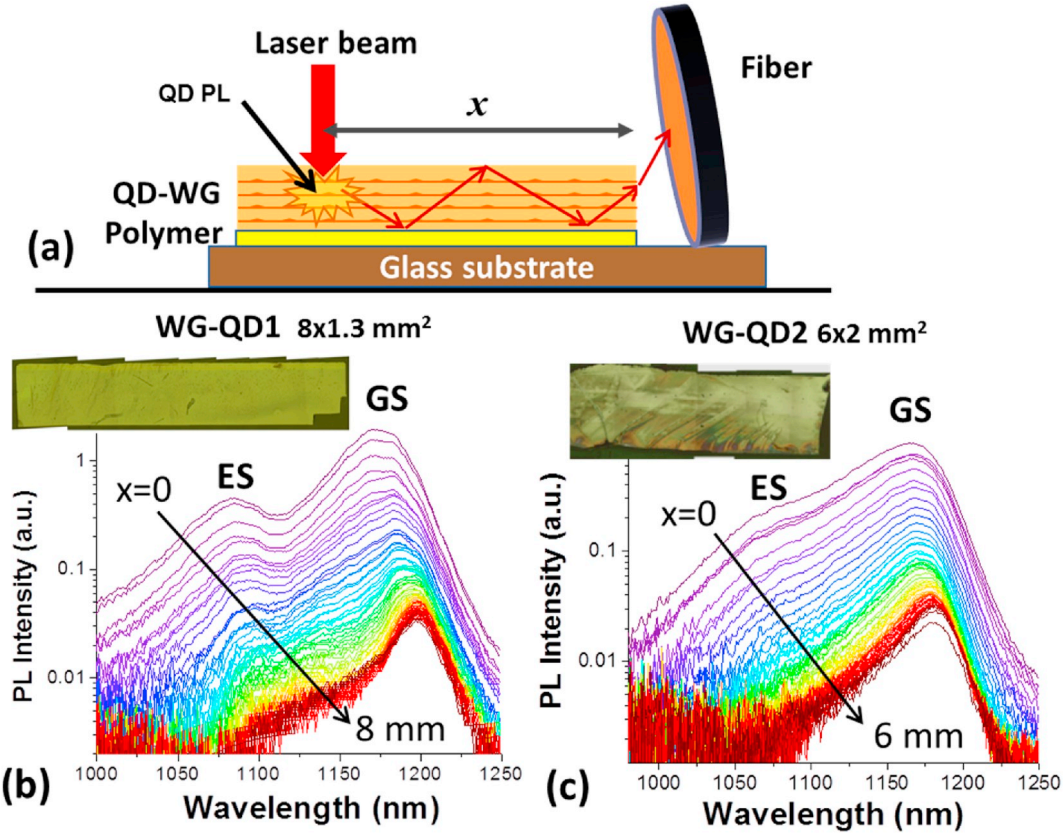

Fig. 6. (a) Experimental setup and (b,c) PL spectra attenuation as a function of the length propagated through the waveguide as the excitation spot moves away from the collecting fiber from: (b) an 8 mm long waveguiding sample with QD1 design (WG-QD1), and (c) from a 6 mm long sample with QD2 design (WG-QD2). GS and ES indicate the QD ground state and excited states emission bands. Insets are optical images of the waveguides.

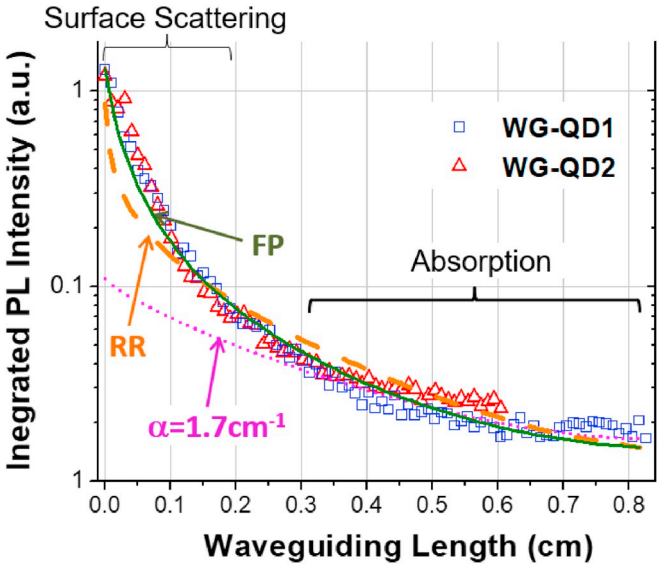

Fig. 7. Integrated PL intensity of WG-QD1 and WG-QD2 samples (symbols) along with the fitting curves (lines). Each symbol is the result of integrating a single PL spectrum from Fig. 6(b and c). Dotted line is a single exponent expression of the Beer–Lambert Law, modified to include waveguided light propagation with a material absorption α = 1.7 cm-1 'RR' dashed line is a Rayleigh-Rice roughness scattering fit with Gaussian roughness of 60 nm and α = 2 cm-1 'FP' solid line is an angle-independent fixed probability photon scattering fit with γ = 14% and α = 0.7 cm^{-1}.

the back surface) light is guided:

$$I_\lambda\left(x\right) = I_{\lambda 0}\iint_{TIR}\sin\theta\left(e^{\frac{-\alpha_\lambda x}{\sin\theta\cos\phi}} + e^{\frac{-\alpha_\lambda(2L-x)}{\sin\theta\cos\phi}}\right)d\theta d\phi, \quad (1)$$

where I_λ refers to the wavelength-specific PL intensity, θ and ϕ are the spherical coordinates of the ray vector (where $\theta = 90^\circ$ and ϕ = 0 correspond to the x direction in Fig. 6(a)), α_λ is the material absorption coefficient at wavelength λ, x refers to the distance from the laser excitation spot to the edge of the WG that is coupled to the fiber (waveguiding length), and L is the length of the waveguide along the x direction. Using this equation, the fit of the integral intensity (Fig. 7, dotted line) with the single parameter $\alpha = 1.7$ cm^{-1} becomes reasonably good for distances larger than ~3 mm. However, at smaller distances, light attenuation is much stronger than expected, even though the fit takes into consideration the increase of the propagation length at large angles ϕ and ($\theta-\pi/2$). Note that the TIR critical angle is small, 17° for GaAs/air and 25° for GaAs/glass interfaces. Therefore, a significant portion of guided light propagates at a high angle to the interfaces.

As the surface of these chemically processed waveguides has a relatively high density of defects including oval defects, etch pits and residues, surface scattering likely affects light propagation. Therefore, our method of analysis, summarized in Eq. (2), incorporates surface scattering with the QD self-absorption from Eq. (1):

$$I_\lambda\left(x\right) = I_{\lambda 0}\iint_{TIR}\sin\theta\left(e^{\frac{-\alpha_\lambda x}{\sin\theta\cos\phi}} + e^{\frac{-\alpha_\lambda(2L-x)}{\sin\theta\cos\phi}}\right)(1-\gamma)^{\left[\frac{x}{h\tan\theta}+\frac{x\tan\phi}{w}\right]}d\theta d\phi \quad (2)$$

where h is the thickness of the waveguide (20, 25 μm) and w is the width of the waveguide (1.3, 2 mm). The scattering term is expressed with a

single unknown coefficient γ, the probability of losing a photon due to scattering in one reflection from the WG surface. The exponent in the brackets gives the integer number of reflections. The scattering coefficient γ for Gaussian-random surfaces with roughness σ is predicted by the Raleigh-Rice (RR) formula [27]:

$$\gamma = \left(\frac{4\pi\sigma\cos\theta}{\lambda}\right)^2 \quad (3)$$

Note that the angle dependence of γ is the result of diffraction on a Fourier component of the surface profile. Alternatively, in cases of surfaces with non-Gaussian randomness, such as single defects, γ may not depend on the ray angle [28]. In this case, each total internal reflection event has a fixed probability (FP) of photon scattering. Both RR and FP curves are shown in Fig. 7, fitted to the integrated PL spectrum. As expected, the additional parameter allows for much better fit of the initial 3 mm of waveguiding length. The RR fit, due to additional angle dependence (Eq. (3)), predicts significantly faster attenuation of high-angle rays. Moreover, the experimentally observed loss of 90% of power over the first 1 mm of waveguiding requires a roughness of about 60 nm, which is an unrealistically large number when compared to visual and AFM inspection (~10 nm). The FP fit provides a better match to the data, and gives a photon scattering probability of $\gamma = 14\%$ per TIR event and the associated low material absorption coefficient of 0.7 cm^{-1}.

As seen in Fig. 6(b and c), the PL spectrum red-shifts as the light propagates in the WG. This is a result of larger absorption coefficients for higher-energy photons in the medium. To evaluate the spectral dependence of the absorption coefficient, fitting using Eq. (2) and the FP model for scattering was used. The attenuation curves for 40 nm wide spectral intervals along with the fits are shown in Fig. 8(a), the resultant spectral dependence of the material absorption coefficient are plotted in Fig. 8(b) for WG-QD1 and WG-QD2. In these fits, the photon scattering probability was wavelength-independent, $\gamma = 14\%$ per TIR event.

Although the 'FP' fits are reasonably good, they account for just two mechanisms of attenuation: QD self-absorption and surface scattering. Other processes can also contribute.

1) Surface scattering returns a portion of energy back into random angle light rays; this process will effectively transfer some energy from the higher-order modes (high angle light rays) with higher attenuation to lower order modes with lower attenuation.
2) Photon recycling in the QD medium will contribute to red-shifting of the spectrum of light propagating in the WG.
3) Due to the large difference between the fiber/cladding diameter (125 μm) and the WG thickness (20, 25 μm), some collection of unguided and scattered light is expected in cases when $x < 200$–400 μm. Thus, the PL intensities from the first several excitation points are slightly higher than the modeled attenuation curves, as can be seen in Figs. 7 and 8(a).

Additional experiments are required to assess the influence of these effects.

Two possible attenuation mechanisms were evaluated for the QD waveguiding samples. The free hole intervalence band absorption coefficient is estimated as 0.4–0.5 cm^{-1} at 1.1 μm wavelength [29] based on doping profile and van der Pauw measurements of carrier concentration discussed in Section 3.1. Rayleigh scattering on QDs in the bulk of the waveguide could result in additional attenuation. To evaluate this, a small-particle Rayleigh approximation was used to find the scattering cross-section, 2×10^{-18} cm^2 [30], with an integral scattering coefficient of as low as 2×10^{-3} cm^{-1}. Both effects were found to be small and were disregarded in this analysis.

Thus, attenuation at small waveguiding length is attributed primarily to wavelength-independent surface scattering. Conversely, at long waveguiding lengths QD self-absorption becomes the dominant source of attenuation. The low material self-absorption obtained here is quite unusual for semiconductors. One reason for this is a relatively low bulk density of QDs (~10^{15} cm^3) and the >200 nm red shift of the QD luminescence from the GaAs band edge.

However, Stranski-Krastanov QD growth mode gives rise to a wetting layer (WL) with a high density of states with transitions closer to those in the QD, which typically result in excess self-absorption. Using an AlAs capping layer to reduce the InAs WL states has recently shown a significant effect on below bandgap photosensitivity [31]. This technique was used in all the samples studied in this paper.

The InAs WL appears as a precursor to the QD self-assembly and is only 1.5–2 ML thick (Fig. 9). This is partially due to fast "freezing" of the growing surface by the ~2 ML of deposited AlAs. The small thickness of the InAs WL, along with the adjacent wide-bandgap AlAs capping, results in the WL energy level being pushed up. Consequently, the bound WL states disappear, which is evidenced by the significant (over an order of magnitude) reduction in the photocurrent close to the QD luminescence spectral interval [31]. This approach also decreases electron exchange between QDs and the GaAs matrix at room and higher temperature, hindering thermal PL quenching.

3.4. Response to alpha particles

We measured the responses of WG-QD1 and WG-QD2 samples, both with integrated photodiodes, to 5.5 MeV alpha particles from a 37 kBq ^{241}Am radioactive source, positioned ~1 cm above the integrated QD scintillation detector. The protective film and the 1 cm of air reduced the alpha particle energy down to about 4 MeV, however the waveguide thickness is large enough to ensure that even 5 MeV alpha particles do

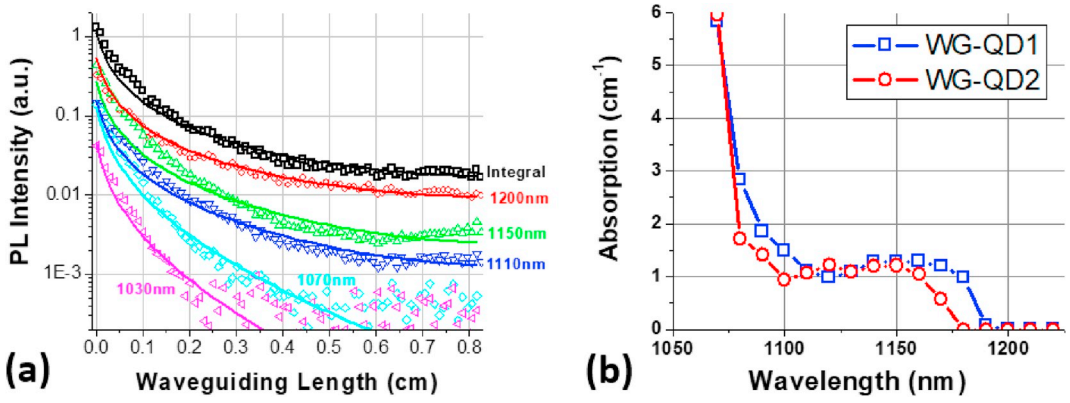

Fig. 8. (a) PL Spectral components from WG-QD1 (Fig. 6b) integrated over 40 nm, fitted with 'FP', an angle-independent fixed probability photon scattering with γ = 14% and material absorption coefficient plotted in (b) for WG-QD1 and WG-QD2.

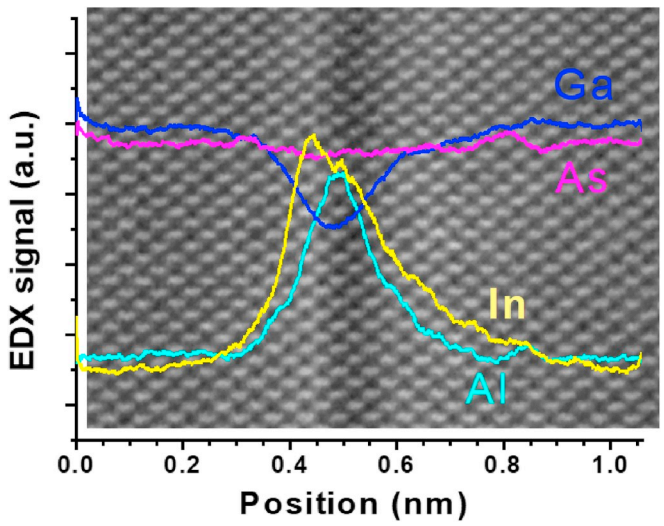

Fig. 9. High-angle annular dark-field (HAADF) cross-sectional micrograph along <110> direction, showing a wetting layer (WL) between the dot, and the overlapped characteristic x-ray intensity profile of the constituent elements across the WL. Bright contrast corresponds to atomic columns: higher-Z elements appear brighter. The Al elemental peak is just 1 ML displaced from the In peak, which raises the transition energy in the InAs WL.

not range out, and that all the kinetic energy of the particle is deposited in the waveguide and converted into the creation of electron-hole pairs. The integrated 0.7 μm thick InGaAs PD was screened from the radioactive source to prevent direct photoionization of the PD by alpha particles.

Fig. 10(a and b) shows responses of WG-QD1 and WG-QD2 to alpha particles as measured from their integrated photodiodes. Both samples had a total multi-stage amplification of ~50×, and the data acquisition rate was about 1 Hz. The graphs contain about 800 and 9000 pulses for WG-QD1 and WG-QD2 respectively. Rise time jitter for both samples is similar: 70 ps as illustrated in the insets. These measurements do not fully reveal statistics of the scintillation photons which should be accounted for. Typically, rise time jitter is characterized using coincidence measurements with two PDs on the same waveguide [32]. However, low signal-to-noise ratio related to high attenuation and excess readout system noise is clearly a limiting factor for the observed rise time jitter, which likely can be further improved.

Even with the relatively high noise levels of the response signal, the statistics of the response decay times were analysed. Fig. 11(a) plots the relation between fitted exponential decay times and the peak pulse voltage for WG-QD1 and WG-QD2. As the extracted decay time of each pulse depends on electronic readout, which is influenced by a specific noise pattern for this pulse, the width of the distribution of fitted decay times reduces with an increase in pulse voltage. At high pulse amplitude, the fitting gives a narrow distribution and thus more accurate average exponential decay time: 0.3 ns for WG-QD1 and 0.4 ns for WG-QD2.

The observed decay times are a combination of the PD, circuit RC, and the QD intrinsic decay times. The slightly longer decay time in WG-QD2 is the result of the 1.4× larger area of the PD on the sample (Fig. 11 (b), insets); the estimation of the PD capacitances gives 3 pF and 4.3 pF for WG-QD1 and WG-QD2 PDs respectively. Previously, a similar WG-QD1 sample was observed to have a 0.28 ns decay time, which is believed to be close to the intrinsic QD luminescence decay time, as it was obtained with a higher frequency (but significantly higher noise) amplification circuit [11].

The amplification of the WG-QD1 and WG-QD2 circuits were separately measured and used to calculate the charge collected by the PDs. The histograms of the collected charge, shown as the number of electrons in a PD response pulse, are presented in Fig. 11(b). The average collected charge is 5.5×10^4 and 7.3×10^4 electrons respectively for WG-QD1 and WG-QD2. As expected WG-QD2, with a 40% larger PD area, collects proportionally more photons from the alpha-particle excitation event. As the average excitation energy per electron-hole pair for the GaAs matrix is 4.35 eV/pair [33] or about 230,000 photons per MeV of deposited energy, the collection efficiency for the two samples is 5.9% and 7.9%, assuming 4 MeV alpha particles interact with the QD/WG. This corresponds to collection of 14,000 and 17,000 scintillation photons per 1 MeV of deposited energy.

It should be noted that although the PDs were screened from the α-source, high initial attenuation limits the collection area to about 2 mm around the PD. This still leaves a chance that alpha particles can hit the PD and directly generate photoelectrons. Given that the pulse decay is affected by both the PD and circuit capacitance, the scintillation pulses and direct photoionization pulses (which may overlap with scintillation signal as the alpha-particle continues its path in the scintillator after deposition of about 0.25 MeV in the PD) appear very similar. In the present setup, the evidence of scintillation can be found in the proportionality of the collected charge to the PD area (Fig. 11(b)). Since the integrated PDs are located on the top of the waveguides, the number of directly photoionized carriers contributing to a signal pulse depends on the PD thickness, but not on its area. In contrast, collection of the scintillation photons by the PD from the waveguide likely scales proportionally with the PD area, meaning a larger area PD will collect more photons, resulting in higher amplitude pulse as observed in Fig. 11(b).

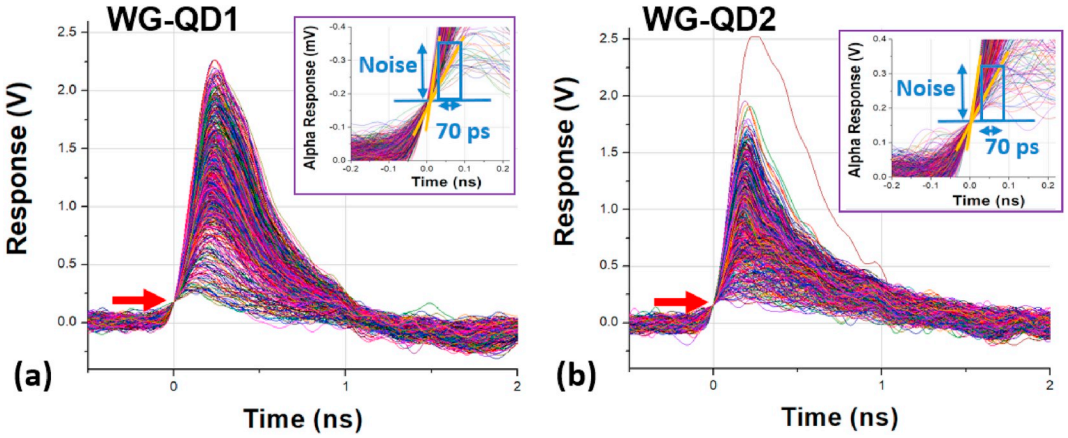

Fig. 10. Alpha particle response of integrated GaAs/InAs QD scintillation detector with (a) WG-QD1 and (b) WG-QD2. The signal was amplified by ~50× and recorded by a 4 GHz oscilloscope; triggering level is indicated with arrows. The insets show the leading edges of the pulses and illustrate a measurable time resolution (jitter) of about 70ps.

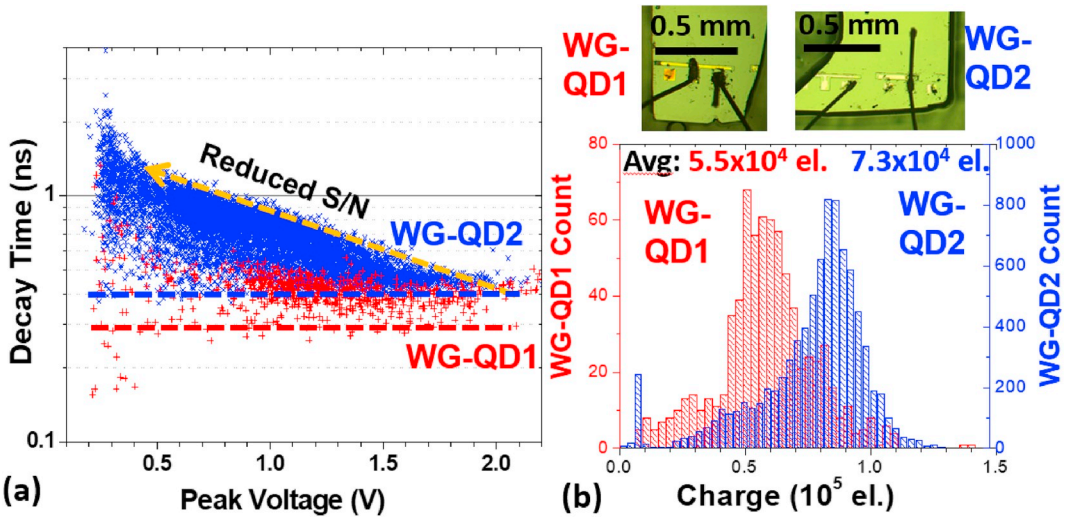

Fig. 11. (a) Fitted exponential decay times vs. peak pulse voltage for WG-QD1 and WG-QD2 samples. Horizontal lines are asymptotic values of the decay time at high amplitude and high signal-to-noise (S/N) ratio. WG-QD2 signal decay is 40% longer due to the higher PD capacitance. (b) Histograms of collected charge from alpha particles by integrated scintillation detectors on WG-QD1 and WG-QD2. The average collected charge is 40% higher in the WG-QD2 sample due to its larger area. Inset shows top-view images of the photodetectors.

The wide histograms and collection efficiencies observed are directly related to high initial attenuation of QD luminescence propagating in the WG, as discussed in Section 3.3. These parameters are insensitive to the dimensions of a waveguide longer than a few millimeters. This effect was also observed as a reduction in the collection rate of alpha particle excitation events when the source was moved a relatively small distance (2–3 mm) from the PD. Low amplitude pulses propagating longer distances were filtered out by the triggering circuit. Optimization of the PD parameters (such as area, thickness, and geometry) with respect to speed and photon collection efficiency for the expected light propagation modes will constitute future research topics.

4. Conclusions

Temperature-dependent photoluminescence, waveguide attenuation, and alpha-particle response measurements were employed to analyze the optical properties of a waveguiding semiconductor scintillation detector, composed of epitaxially grown InAs quantum dots (QDs) in a GaAs semiconductor matrix. QD PL in our best sample shows ~60% efficiency at room temperature and 20% efficiency at 463 K, showing the benefits of optimizing the p-type modulation doping profile to further improve PL thermal quenching. Analysis of the attenuation of the QD waveguide shows predominant surface scattering over the first 2–3 mm of light propagation and low (~1 cm^{-1}) self-absorption at longer distances, after the decay of higher-order modes (high angle light rays). Measured responses to 5.5 MeV alpha particles from the integrated InAs QD/WG show an extremely fast decay constant at high pulse amplitudes of 300 ps, and a 70 ps time resolution (limited by circuit noise and bandwidth) with a collection efficiency of 17,000 photons per 1 MeV of deposited energy.

CRediT authorship contribution statement

K. Dropiewski: Methodology, Software, Investigation, Formal analysis, Writing - original draft, Writing - review & editing, Visualization. **A. Minns:** Validation, Investigation, Resources. **M. Yakimov:** Conceptualization, Methodology, Resources. **V. Tokranov:** Conceptualization, Investigation, Resources. **P. Murat:** Validation, Formal analysis, Writing - original draft. **S. Oktyabrsky:** Conceptualization, Writing - original draft, Writing - review & editing, Visualization, Supervision, Project administration, Funding acquisition.

Acknowledgments

The authors would like to acknowledge support from the National Science Foundation under award DMR-1511708637 and the U.S. Department of Energy, Office of Science under Award DE-SC0019031.

References

[1] S. Oktyabrsky, M. Yakimov, V. Tokranov, P. Murat, Integrated semiconductor quantum dot scintillation detector: ultimate limit for speed and light yield, IEEE Trans. Nucl. Sci. 63 (2016) 656–663.
[2] A. Ronzhin, M. Albrow, M. Demarteau, S. Los, S. Malik, A. Pronko, E. Ramberg, A. Zatserklyaniy, Development of a 10ps level time of flight system in the fermilab test beam facility, Nucl. Instrum. Methods Phys. Res. Sect. A Accel. Spectrom. Detect. Assoc. Equip. 623 (2010) 931–941.
[3] M. Conti, L. Eriksson, H. Rothfuss, C.L. Melcher, Comparison of fast scintillators with TOF PET potential, IEEE Trans. Nucl. Sci. 56 (2009) 926–933.
[4] D.J. Kadrmas, M.E. Casey, M. Conti, B.W. Jakoby, C. Lois, D.W. Townsend, Impact of time-of-flight on PET tumor detection, J. Nucl. Med. 50 (2009) 8.
[5] P. Lecoq, Pushing the limits in Time-Of-Flight PET imaging, IEEE Trans. Radiat. Plasma Med. Sci. 1 (2017) 473–485.
[6] K. Doroud, M. Williams, A new approach for improved time and position measurements for TOF-PET: time-stamping of the photo-electrons using analogue SiPMs, Nucl. Instrum. Methods Phys. Res. Sect. A Accel. Spectrom. Detect. Assoc. Equip. 849 (2017) 16–19.
[7] S.E. Derenzo, M.J. Weber, E. Bourret Courchesne, M.K. Klintenberg, The quest for the ideal inorganic scintillator, Natl. Instrum. Methods Phys. Res. A 505 (2003) 6.
[8] S. Gundacker, R.M. Turtos, E. Auffray, P. Lecoq, Precise rise and decay time measurements of inorganic scintillators by means of X-ray and 511 keV excitation, Nucl. Instrum. Methods Phys. Res. Sect. A Accel. Spectrom. Detect. Assoc. Equip. 891 (2018) 42–52.
[9] P. Lecoq, Development of new scintillators for medical applications, Nucl. Instrum. Methods Phys. Res. Sect. A Accel. Spectrom. Detect. Assoc. Equip. 809 (2016) 130–139.
[10] M. Nikl, A. Yoshikawa, Recent R&D trends in inorganic single-crystal scintillator materials for radiation detection, Adv. Opt. Mater. 3 (2015) 463–481.
[11] K. Dropiewski, A. Minns, M. Yakimov, V. Tokranov, P. Murat, S. Oktyabrsky, Ultrafast Waveguiding Quantum Dot Scintillation Detector. Nuclear Instruments and Methods in Physics Research Section A: Accelerators, Spectrometers, Detectors and Associated Equipment, 2018.
[12] K. Gündoğdu, K. Hall, T.F. Boggess, D. Deppe, O. Shchekin, Ultrafast electron capture into p-modulation-doped quantum dots, Appl. Phys. Lett. 85 (2004) 4570–4572.
[13] L. Zhang, T.F. Boggess, D. Deppe, D. Huffaker, O. Shchekin, C. Cao, Dynamic response of 1.3-μm-wavelength InGaAs/GaAs quantum dots, Appl. Phys. Lett. 76 (2000) 1222–1224.
[14] D.L. Rode (Ed.), Semiconductors and Semimetals, Academic Press, New York, 1975.
[15] O. Stier, M. Grundmann, D. Bimberg, Electronic and optical properties of strained quantum dots modeled by 8-band k·p theory, Phys. Rev. B Condens. Matter Mater. Phys. 59 (1999) 5688–5701.
[16] E. Schubert, Light Emitting Diodes, Cambridge University Press, 2006.

[17] E. Yablonovitch, T. Gmitter, J. Harbison, R. Bhat, Extreme selectivity in the lift-off of epitaxial GaAs films, Appl. Phys. Lett. 51 (1987) 2222–2224.
[18] V. Tokranov, M. Yakimov, A. Katsnelson, K. Dovidenko, M. Lamberti, S. Oktyabrsky, Shape engineered InAs QuantumDots with stabilized electronic properties, Mater. Res. Soc. Symp. Proc. 737 (2003).
[19] L.-H. Chien, A. Sergeev, V. Mitin, S. Oktyabrsky, Quantum dot photodetectors based on structures with collective potential barriers, Proc. SPIE 7608 (2010), 760826-760826-760828.
[20] M. Yakimov, A. Sergeev, V. Pogrebnyak, A. Varghese, V. Tokranov, G. Thomain, N. Vagidov, V. Mitin, S. Oktyabrsky, Engineering of absorbing medium for quantum dot infrared photodetectors, Proc. SPIE 8876 (2013), 88760V-88760V-88769.
[21] A. Sergeev, V. Mitin, N. Vagidov, K. Sablon, Charged quantum dots for high-efficiency photovoltaics and IR sensing, in: S. Luryi, J. Xu, A. Zaslavsky (Eds.), Future Trends in Microelectronics: Frontiers and Innovations, 2013, pp. 244–253.
[22] P. Bhattacharya, S. Ghosh, S. Pradhan, J. Singh, Z.-K. Wu, J. Urayama, K. Kim, T. B. Norris, Carrier dynamics and high-speed modulation properties of tunnel injection InGaAs-GaAs quantum-dot lasers, IEEE J. Quantum Electron. 39 (2003) 952–962.
[23] S. Oktyabrsky, M. Lamberti, V. Tokranov, G. Agnello, M. Yakimov, Room-temperature defect tolerance of band-engineered InAs quantum dot heterostructures, J. Appl. Phys. 98 (2005), 053512.
[24] I. Novikov, N.Y. Gordeev, L.Y. Karachinskii, M. Maksimov, Y.M. Shernyakov, A. Kovsh, I. Krestnikov, A. Kozhukhov, S. Mikhrin, N. Ledentsov, Effect of p-doping of the active region on the temperature stability of InAs/GaAs QD lasers, Semiconductors 39 (2005) 477–480.
[25] P.V. Nikitin, D.D. Stancil, E.A. Erosheva, Estimating the number of modes in multimode waveguide propagation environment, in: IEEE International Symposium on Antennas and Propagation (APSURSI). 2011, IEEE: Spokane, WA, USA, 2011.
[26] V. Tokranov, M. Yakimov, A. Katsnelson, M. Lamberti, S. Oktyabrsky, Enhanced thermal stability of laser diodes with shape-engineered quantum dot medium, Appl. Phys. Lett. 83 (2003) 833–835.
[27] P.K. Tien, Light waves in thin films and integrated optics, Applied optics 10 (1971) 2395–2413.
[28] J.C. Stover, Optical Scattering: Measurement and Analysis, third ed. ed., SPIE, Bellingham, WA, 1995.
[29] J. Taylor, V. Tolstikhin, Intervalence band absorption in InP and related materials for optoelectronic device modeling, J. Appl. Phys. 87 (2000) 1054–1059.
[30] A. Cox, A.J. DeWeerd, J. Linden, An experiment to measure Mie and Rayleigh total scattering cross sections, Am. J. Phys. 70 (2002) 620–625.
[31] A. Varghese, M. Yakimov, V. Tokranov, V. Mitin, K. Sablon, A. Sergeev, S. Oktyabrsky, Complete voltage recovery in quantum dot solar cells due to suppression of electron capture, Nanoscale 8 (2016) 7248–7256.
[32] S. Derenzo, W.-S. Choong, W. Moses, Fundamental limits of scintillation detector timing precision, Phys. Med. Biol. 59 (2014) 3261–3286.
[33] T. Kobayashi, T. Sugita, M. Koyama, S. Takayanagi, Performance of GaAs surface-barrier detectors made from high-purity gallium arsenide, IEEE Trans. Nucl. Sci. 19 (1972) 324–333.